ELSEVIER

Contents lists available at ScienceDirect

Carbon Trends

journal homepage: www.elsevier.com/locate/cartre



Enhanced storage performance of a low-cost hard carbon derived from biomass

Chen Wang a,b, Debasis Sen c,d, Vinod K. Aswal c,d, Lan Weiguang e, Palani Balaya a,*

- ^a Department of Mechanical Engineering, College of Design and Engineering, National University of Singapore, 117575, Singapore
- ^b Suntar Membrane Technology (Xiamen) Pte. Ltd. Xiamen-361022, Fujian, China
- ^c Solid State Physics Division, Bhabha Atomic Research Centre, Trombay, Mumbai 400085, India
- ^d Homi Bhabha National Institute, Anushaktingar, Mumbai 400094, India
- e Xiamen University, Xiamen 361005, Fujian, China

ARTICLE INFO

Keywords: Sodium-ion battery Hard carbon Anode Plateau capacity SANS Storage mechanism

ABSTRACT

Hard Carbon is the most widely used negative electrode material for sodium-ion batteries today. Achieving high storage capacity and increasing the plateau capacity, as opposed to the sloping profile, are crucial for enhancing energy density of the full cells. While several publications address the synthesis of hard carbon, the economic viability for commercial scale-up hinges on the choice of precursors. In this study, we report the electrochemical properties of hard carbon derived from two biomass precursors, sugarcane waste (bagasse) and corn waste, and compare their performances with commercially available hard carbon. The hard carbon derived from bagasse delivers a capacity of 307 mAh/g at C/10 rate and retains approximately 234 mAh/g at 3C discharge rate. We integrate surface area, pore size distribution, Raman spectroscopy, small-angle X-ray and neutron scattering data to elucidate the sodium storage mechanism in these hard carbon samples. Correlated graphitic domains with hexagonal ordering along with fractal like agglomeration of the nanosheets are quantified. The high plateau capacity of the bagasse-derived hard carbon is attributed to the characteristic morphology and size distribution of the nanosheets and their nature of agglomeration.

1. Introduction

Compared to the mature lithium-ion battery (LIB) technology, sodium-ion battery (SIB) is still in its early stages, with rapid development efforts aimed at commercialization. SIB has garnered significant attention as a potential substitute for LIB, particularly for large-scale stationary storage applications mainly due to the abundance of sodium element [1] and its similar working principles to LIB.

Nowadays, LIBs generally use graphite as anode active material, known for its low toxicity, acceptable price, and high abundance. However, using graphite as anode in SIBs with conventional carbonate-based electrolytes such as $NaPF_6$ in EC:PC etc., has been proven to be unfavorable [2]. Sodium-graphite intercalation compounds (Na-GICs) exhibit low energetic stability, indicating weak chemical bonding between Na-ion and graphite structure. Consequently, non-graphitizable carbon, known as 'hard carbon' (HC), is the preferred anode material for SIBs due to its high storage capacity, low working potential and cycling stability. Additionally, HC can be sourced from environmentally

friendly and inexpensive renewable bio-sources, offering advantages in cost and large-scale production.

HC is typically obtained through a thermal or chemical process of pure organic compounds or biomass-derived precursors, the process is generally referred to as 'carbonization'. During carbonization, volatile molecules like $\rm H_2O$, $\rm CO_2$, and $\rm N_2$ are released [3,4], resulting in hard carbon characterized by high porosity [5], low particle density [6,7], and low bulk powder density, while retaining the original micromorphology [8]. The carbonization process involves several concurrent reactions, such as dehydrogenation, condensation, hydrogen transfer, and isomerization. Unlike graphitizable carbon, the macromolecular structure of the precursor for non-graphitizable carbon persists without converting into a fluid phase upon heat treatment. Consequently, the derived HC samples maintain the same microstructure and morphology as the precursor material, but with lower bulk density.

Recently, synthesizing amorphous carbons from abundant waste biomasses, such as peat moss, banana peel, pomelo peel, peanut shell, shaddock peel, argan shell, and so on [9-15], as well as

E-mail address: mpepb@nus.edu.sg (P. Balaya).

^{*} Corresponding author.

carbon-containing extracts like sucrose, gelatin, α -cellulose, urea, and so on [16-22], have drawn much interest.

Cheng et al. [23] used carbonized coconut shell as raw material for HC synthesis and reported the relationship between thermal treatment temperature, crystal structure and electrochemical performance. It was found that HC prepared at $1300\,^{\circ}\text{C}$ exhibited a specific capacity of 224 mAh/g after $100\,\text{cycles}$ at a current density of $100\,\text{mA/g}$. Song et al. [24] demonstrated that homogeneous P-doping of the coal-based micronsized HC increased the low-voltage plateau capacity during continuous cycling due to the enlarged interlayer spacing. However, they reported that the high-voltage sloping capacity does not change obviously. The plateau capacity of this doped hard carbon after 500 cycles at $100\,\text{mA/g}$ was found to be $13\,^{\circ}\text{M}$ larger than that of unpretreated HC. Kamiyama et al. [25] introduced a novel HC synthesis method by heating a freeze-dried mixture of magnesium gluconate and glucose, achieving an unusually large storage capacity of $478\,\text{mAh/g}$ with a first cycle coulombic efficiency of $88\,^{\circ}\text{M}$ in aprotic Na cells.

In this study, two biomass precursors, bagasse and corn waste, were chosen for HC synthesis. Bagasse, the dry pulpy fibrous residue remaining after sugarcane stalks are crushed to extract their juice, is a by-product of the cane sugar industry with a significant production level. For every 10 tons of sugarcane crushed, a sugar factory produces nearly three tons of wet bagasse [26]. Similarly, corn waste is also abundantly produced. For instance, 9.6 \times 10 7 acres of land in the U.S. dedicated to corn production [27,28]. Thus, the choice of precursors in this study, bagasse and corn waste, are readily available and cost-effective industrial waste materials.

In this study, a simple synthesis approach to produce HC from these two precursors is adopted. Material characterization and electrochemical performance analysis were conducted on the prepared HC samples to understand the relation between structural properties and electrochemical performances. The morphology and structure of the HC materials were examined using X-ray diffraction (XRD), small-angle Xray scattering (SAXS), small-angle neutron scattering (SANS), scanning electron microscope (SEM), Raman spectroscopy, and BET surface area measurement. Thermogravimetric and differential thermogravimetric (TG-DTA) analyses characterized the pyrolysis behavior. Sodium halfcells were made to examine the electrochemical sodium storage performances of the HC samples. Compared to HC sample synthesized from dried corn waste and a commercial sample, HC produced from dried bagasse exhibited higher storage capacity with larger plateau capacity. To the best of our knowledge, this study is among the most relevant combining SANS and SAXS results for structural analysis to explain the observed high plateau-capacity in bagasse-derived HC samples.

2. Experimental section

2.1. Materials synthesis

The hard carbon (HC) samples were prepared from sugarcane waste (bagasse) and corn waste through a simple synthesis route. The process started from drying the bagasse and corn waste at 120 $^{\circ}\text{C}$ for 72 h. Afterwards, both the precursors were ground into fine powder. Each sample was then introduced in a tubular furnace under a flow of high purity argon gas at 100 mL/min and heated by 5 $^{\circ}\text{C}$ per minute to a targeted temperature, annealed for 1 h then ambient-cooled to room temperature. The annealing temperature in this study ranged between 1000 and 1400 $^{\circ}\text{C}$. The temperature range was chosen based on thermal gravimetric analysis (TGA) results which can be found in the later section. The prepared samples were denoted DB-T (for dried bagasse) and DC-T (for dried corn), while T refers to the annealing temperature.

2.2. Materials characterization

Powder XRD was performed with a Bruker D8 ADVANCE ECO X-ray powder diffractometer using Cu-K $_{\alpha}$ radiation operated at 40 kV and 25

mA. Surface morphology and particle size were observed using a JEOL JSM-7000F Field-Emission Scanning Electron Microscope (FESEM). Nitrogen-physisorption characterization was recorded at 77 K using a Nova 2200e surface area analyzer (Quantachrome, USA). Prior to this BET surface area measurement, the samples were degassed in vacuum at 130 °C for 12 h. Raman spectroscopy was performed using a Modular Raman Spectrometer (Jobin Yvon, HORIBA) with a laser (Stellar Pro Argon-ion) excitation wavelength of 514 nm (Green). SAXS measurements were performed using a laboratory based SAXS instrument. The sample to detector distance was nearly 1 m and CuK_{α} X-ray was used as probing radiation. Radial averaging was performed on the collected 2D data to obtain variation of scattering intensity I(Q) with wave vector transfer (Q). SANS measurements were performed with two sets of instruments [29,30]. A pin hole collimation-based SANS facility (SANS-I) was used to collect the data in the Q range of 0.15 nm⁻¹ to 2.5 nm⁻¹. Data in the lower scattering vector Q range is obtained using a medium resolution double crystal based small-angle neutron scattering (MSANS) instrument (SANS-II) ²⁷ at Trombay, India [29,30]. Data from two facilities were normalized at the common Q region to obtain consolidated scattering profile over a Q range of 0.005 to 2.5 nm⁻¹. Data with a higher O range were obtained using the small and wide-angle neutron scattering instrument (TAIKAN) at J-PARC, Japan [31].

2.3. Electrochemical measurements

The negative electrodes were prepared by mixing the synthesized hard carbon samples with sodium carboxymethyl cellulose (CMC) binder (Alfa Aesar) in the weight ratio of 95:5 using Milli-Q water as solvent. The slurry was then coated on an etched aluminum foil of 15 μm thickness and dried in a vacuum oven at 110 $^{\circ} C$ for 12 h. The active material loading was around 3 mg/cm². A glass fiber filter (Whatman) was used as separator and an in-house prepared non-flammable 1 M NaBF4 in tetraglyme [32] was used as electrolyte. All the electrochemical tests were performed using CR2016 type coin cells via an Arbin battery tester (#MSTAT) taking 372 mAh/g as theoretical Na storage capacity for HC.

3. Results and discussion

3.1. Structural and morphological analysis

Dried bagasse and corn cob waste materials were used as precursors for the synthesis of carbonaceous materials. The high temperature decomposition of both the precursors were recorded using TGA under argon atmosphere and results are shown in Fig. 1. There was very minimal weight loss above 400 $^{\circ}\text{C}$ for both the precursors and the precursors' weight loss becomes negligible after 600 $^{\circ}\text{C}$. At 1000 $^{\circ}\text{C}$, there was 14 % weight remaining for dried bagasse and 20 % remaining for corn waste. Thus, there was indication of higher yield after carbonization for corn waste compared to bagasse.

Fig. 2 shows pictures taken on bagasse and corn cob waste precursors before and after annealing at 1400 $^{\circ}$ C. According to these pictures, the HC product was able to retain most of the precursor's morphology. As for bagasse (Fig. 2(a) and (b)), the precursor appeared in short fibrous segments while the derived HC sample retained analogous appearance right after annealing. The same happened in the case of corn cob waste.

In addition to the hard carbon samples, obtained from the above-mentioned precursors, a commercial hard carbon sample (Type C) was selected for comparison of their sodium storage performances. Fig. 3 shows the Field Emission Scanning Electron Microscopy (FESEM) images of these three hard carbon (HC) samples, DB-1400, DC-1400, and Type C. From the low magnification images shown in Fig. 3(a), (c), and (e), it can be seen that DC-1400 and Type C HC samples have a morphology consisting of small particles of around 10 μ m. The size distribution is more regular in Type C HC as compared to DC-1400. For the case of DB-1400, the particles are irregular, and characteristics of the

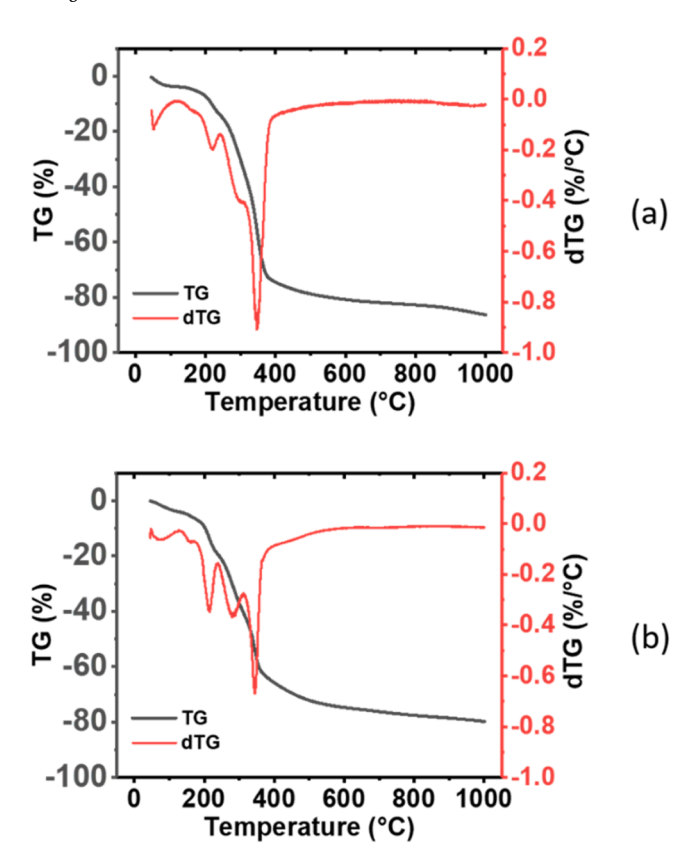


Fig. 1. TGA results for (a) dried bagasse and (b) dried corn cob waste.

precursor are retained after carbonization, even though the yield sample is hand-grounded thoroughly.

Moreover, when the samples are viewed using FESEM at high magnification, pores with diameter of 1 μm can be seen clearly in DB-1400 sample (Fig. 3(b)), originating from the same pore structure of bagasse precursor [8]. The presence of such pores can increase the

contact area between the sample and electrolyte thus favors wetting process of the electrolyte, which leads to better access to the active material by Na-ions in the electrolyte. Similar pores are also present in DC-1400 and Type C samples, but it is clear from the FESEM images that the number density of those pores is low in these two samples.

Powder X-ray diffraction (XRD) patterns for the three tested samples, shown in Fig. 4, give relevant information about the structure of these materials. Only two predominant peaks are seen at 2θ , 23° and 44° , due to the X-rays being diffracted by the crystalline planes of graphitized and turbostratic structures of the HC material. Other components, like amorphous and highly disordered structures of the hard carbon materials, cannot be identified from XRD measurements. The diffraction patterns show that all the three materials exhibit two broad peaks, indicating that all the carbonaceous samples have a disordered structure [33]. The peak around 23° , which is attributed to the crystallographic plane (002), tend to shift to higher angles in the sequence of Type C, DC-1400, and DB-1400. That indicates that the distance between graphene sheets (d_{002}) decreases and the stacking height together with the number of stacked graphene increases [33].

The nitrogen-physisorption characteristics and their respective BJH pore size distributions for the three samples are shown in Fig. 5. All samples feature a well-defined hysteresis loop, which is attributed to a Type-IV isotherm associated with a mesoporous nature [34]. BET surface area of the samples, DB-1400, DC-1400, and Type C, are 74.43 m²/g, 1.50 m²/g, and 1.90 m²/g, respectively (Table 1). Results from BET and BJH analysis (Table 1 and Fig. 5) are consistent with the FESEM image. DC-1400 and Type C HC have similar structures as viewed from FESEM images. Value of BET surface area, total pore volume, average pore size, and the pore volume distribution are similar for these two samples as well. On the other hand, DB-1400 sample has higher BET surface area as well as total pore volume compared to the other two samples, which results in better absorption of electrolyte by this HC material.

To better understand the micro-structure of the HC samples, small-angle neutron scattering (SANS) measurements was carried out and the results are shown in Fig. 6. The medium resolution SANS (MSANS) and conventional SANS data were normalized at common Q region to obtain the combined scattering profile extending over nearly three

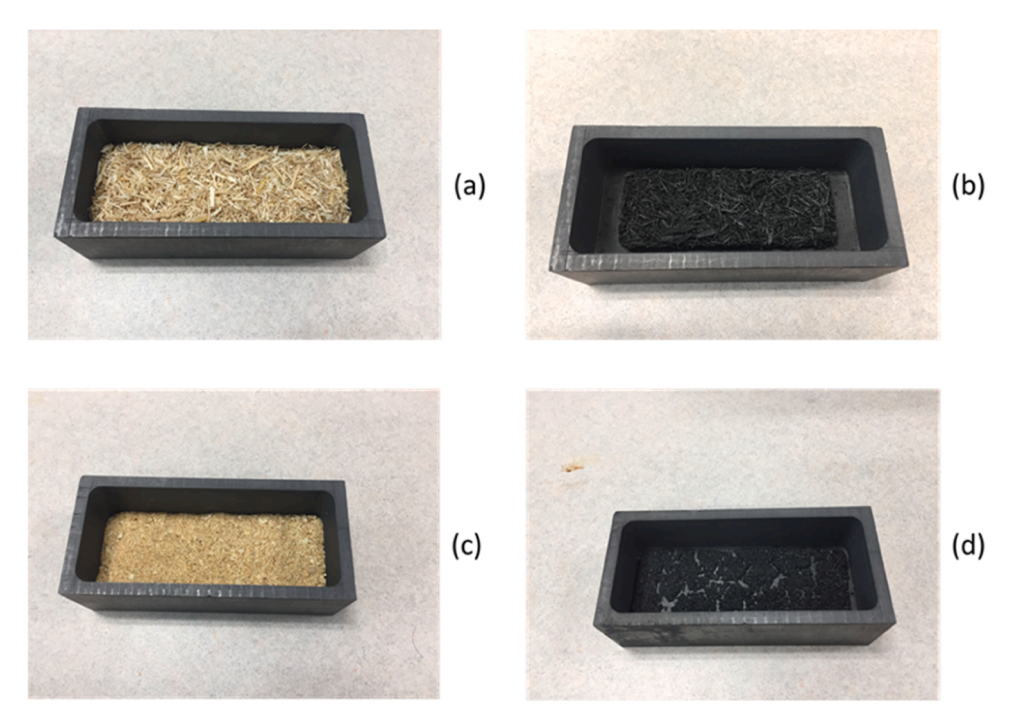


Fig. 2. Picture of bagasse precursor (a) before and (b) after; and corn cob waste (c) before and (d) after annealing at 1400 °C.

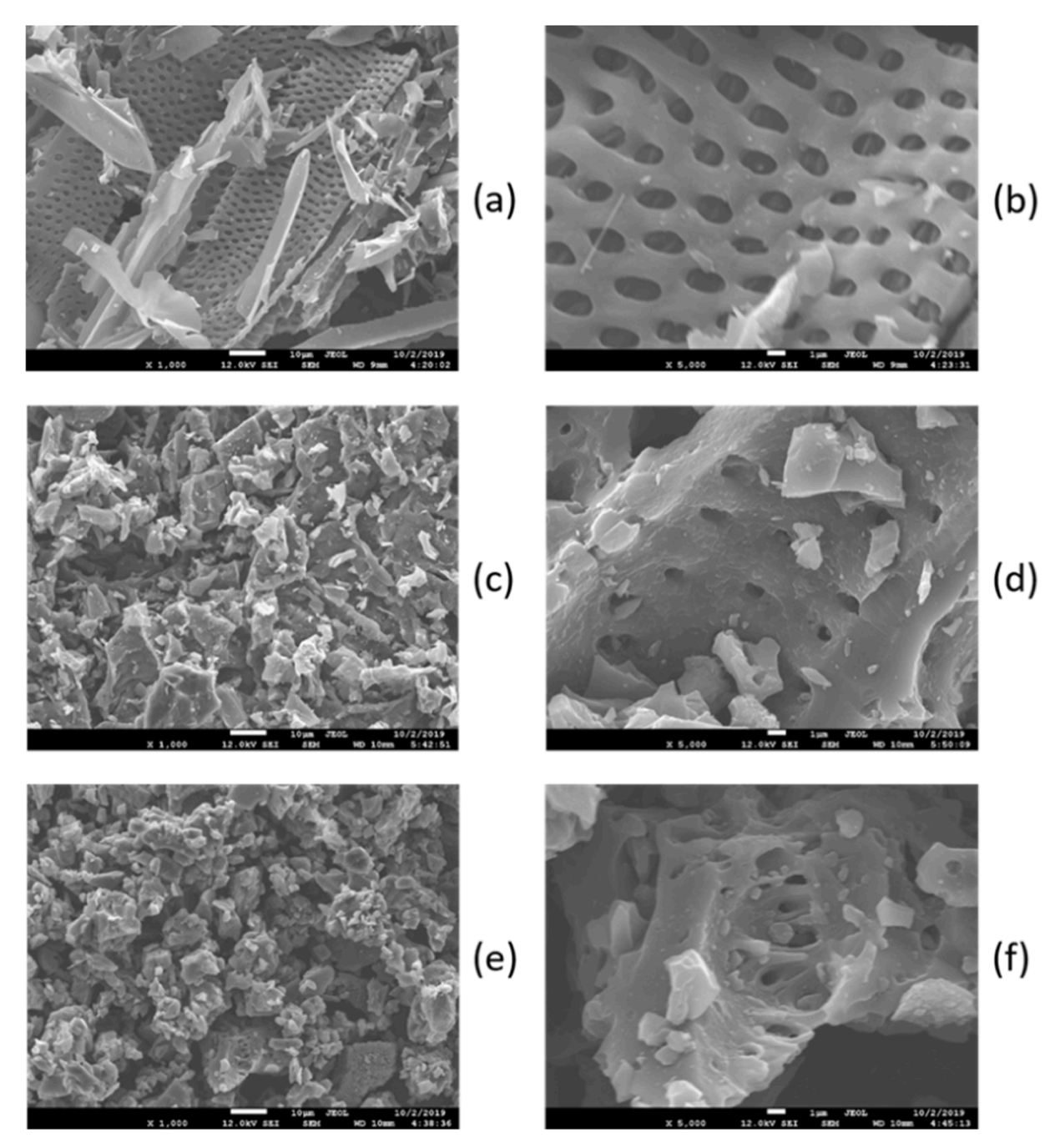


Fig. 3. FESEM image of hard carbon sample DB-1400 at (a) 1000x and (b) 5000x; DC-1400 at (c) 1000x and (d) 5000x; and Type C at (e) 1000x and (f) 5000x.

decades in O (Fig. 6a).

The power-law type variation of scattering intensity in the Q range $(0.03-0.5~\text{nm}^{-1})$ is observed from the data shown in Fig. 6(a) and (b). Additionally, Fig. 6(b) also shows correlation peaks from graphitic domains. Data represented in Fig. 6(b) were fitted to the following model using with SASfit software [35]:

$$I(q) = N \cdot P_{sheet}(q) S_{fractal}(q) + C \cdot S_{hexagonal}(q) + Background$$
 (1)

In Eq. (1), $P_{sheet}(q)$ represents the form factor of disk-shaped particles/pores. $S_{fractal}(q)$ represents the fractal-like structure factor that explains the low q power law scattering. N is the scale factor, independent of Q and depends on number density and scattering contrast. The second term has been considered to take into account the graphitic correlation in the samples as was observed in the higher Q regime in the data obtained from small-and wide-angle scattering spectrometer, TAIKAN, J-

PARC. $S_{hexagonal}(q)$ represents the structure factor owing to the correlated graphitic domains with hexagonal ordering. Since small-angle scattering data, in general, originates owing to the presence of the minority [36] mesoscopic inhomogeneities (Babinet principle), for closely packed samples. Scattering data are expected to provide the information about the pores; in contrast, for loosely packed samples, data are supposed to provide the information about the particles. Therefore, to understand the fitted data, tap density together with BET analysis results should be viewed as complementary. The solid line in Fig. 6(b) represents the fit of the model to the experimental data.

The parameters from the fit are shown in Table 1. The fractal dimension [37] reflects the power-law characteristic of the data in lower Q regime. The value of fractal dimension for Type C HC is close to 3 (2.95), which shows that the material has a consolidated structure. In contrast, the value of fractal dimension for DB-1400 and DC-1400 is

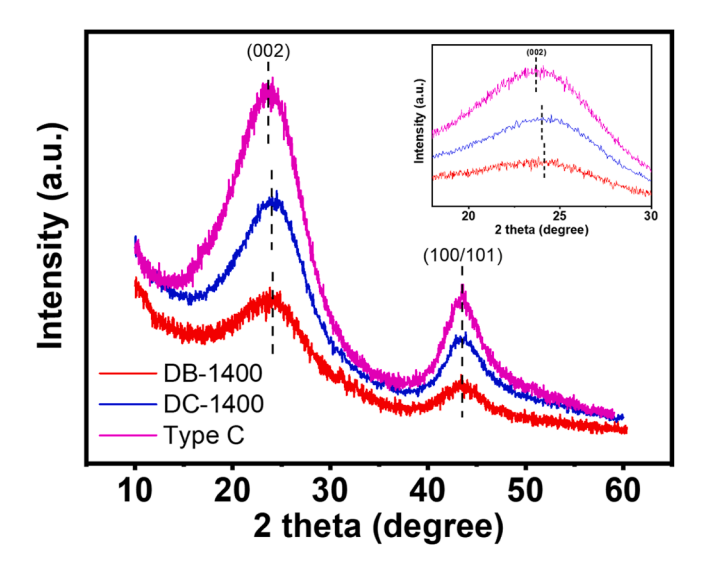


Fig. 4. PXRD patterns of DB-1400, DC-1400, and type C hard carbon samples.

much lower than 3. Therefore, these two materials have more opened structures as compared to Type C. This is in-line with BET results. Moreover, the tap density for DB-1400, DC-1400 and Type C HC sample is 233.7, 348.8, and 675.4 kg/m 3 , respectively. This also agrees with the estimated fractal dimension, as the one with the highest fitted value (Type C HC) has the most consolidated structure and shows the highest tap density.

The data fitted with high Q range results from Fig. 6 shows properties of graphitic nano-domains [38] instead of pores since the HC sample is very loosely packed. Especially in the case of DB-1400, where its tap density is very low, mesopores (empty space) are the majority species while graphitic nano-domains are minority in a specific volume of the sample. In this scenario, DB-1400 with the lowest N value, which represents the number density of the minority (graphitic nano-domains), should have the most open structure with a lot mesopores in between the graphitic nano-domains. This agrees with the electrochemical performance as discussed later, where DB-1400 shows highest plateau capacity which is resulted from Na-ion intercalation into these mesopores.

Fig. 7 shows the Raman spectra of the HC samples. Two broad characteristic bands of defective or disordered carbon around 1340 cm⁻¹ (D-band), and 2D vibrations of pairs of sp² bonded carbon atoms around 1590 cm⁻¹ (G-band) can be found in the patterns for all three samples.

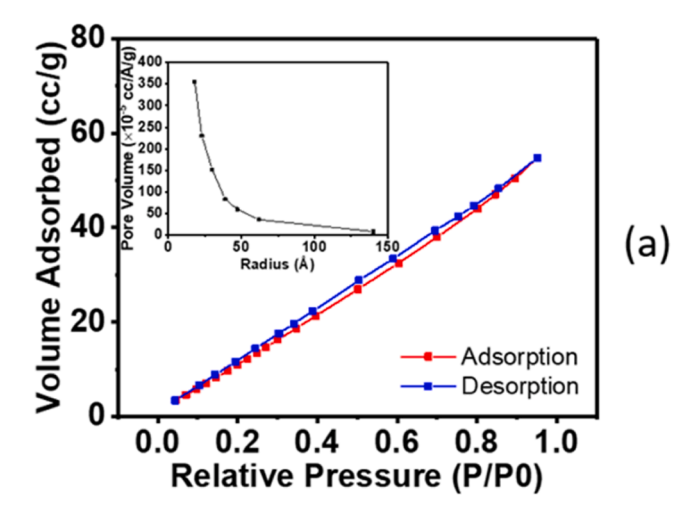
These peaks were fitted using a Lorentzian function to determine the I_D/I_G ratio, while I_D and I_G refer to the integration of D-peak and G-peak, respectively. Detailed fitted results can be found in Table 2. Lower value of the I_D/I_G ratio for DB-1400 sample suggests that disordered graphene sheets tend to form small graphitic regions in this sample. L_a parameter, which represents the lateral size of the graphitic crystalline [39], is calculated based on the equation [39]:

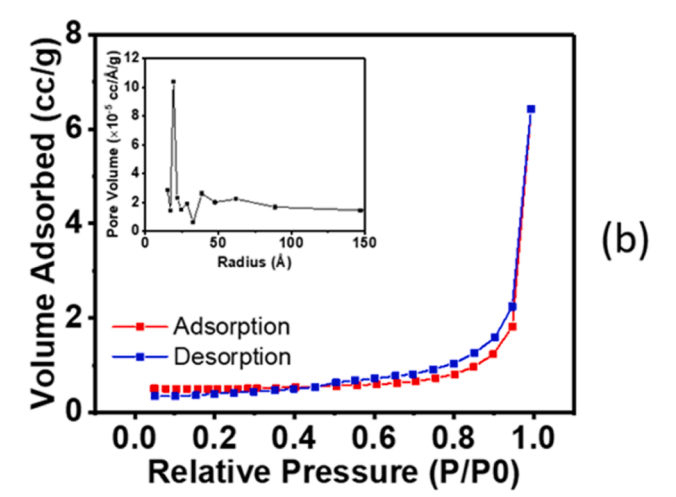
$$L_a(nm) = (2.4 \times 10^{-10}) \times \lambda(nm)^4 \times \left(\frac{I_D}{I_G}\right)^{-1}$$
 (2)

The parameter λ in Eq. (2) represents the laser wavelength, which in this case is 514 nm. Higher L_a parameter for DB-1400 sample (Table 2) indicates the graphitic regions are larger as compared to the other two samples [33].

3.2. Electrochemical performances

Half-cells of DB-T and DC-T samples were cycled between 0.01 V and 1.5 V. HC electrode active material loading was targeted at 3 $\mbox{mg/cm}^2$ which is at the same level of the electrode prepared for commercial 18,650 cylindrical cell. Electrolyte used was an in-house prepared non-flammable 1 M NaBF4 in tetraglyme electrolyte.





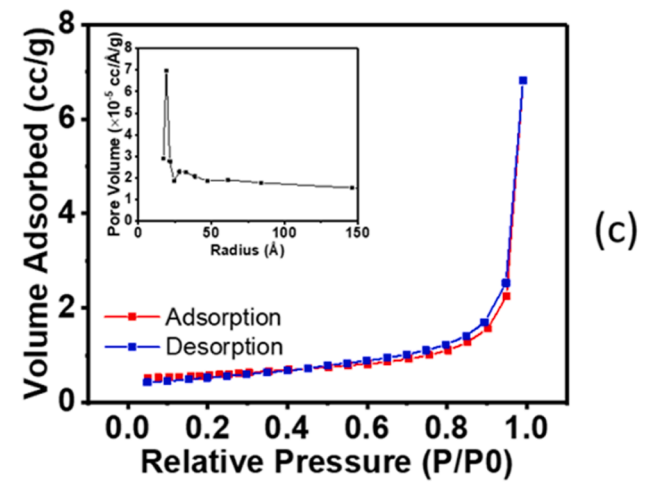


Fig. 5. Nitrogen physisorption isotherms of (a) DB-1400, (b) DC-1400, and (c) type C HC samples with inset showing BJH pore size distribution.

Fig. 8 shows the first and second galvanostatic charge-discharge profiles. All the profiles demonstrate two distinct potential regions: a slope domain in the potential window between 1.5 and 0.15 V assigned to the intercalation of Na^+ in the interlayer space between graphene sheets in the graphitic nano-domains; and a wide plateau below 0.15 V attributed to the insertion of Na^+ in the pores [2,33,40,41]. It is clearly shown that among the two sets of DB-T (Fig. 8(a) and (b)) and DC-T

Table 1
Results obtained by BET surface area analysis, BJH pore size and volume analysis and fitting of SAXS and SANS data.

Sample	BET surfaces area (m ² /g)	Total pore volume (cc/g)	Average pore size (Å)	N	Sheet thickness (nm)	Sheet diameter (nm)	Fractal lower cut-off (nm)	Fractal upper cut-off (nm)	Fractal dimension
DB- 1400	74.43	0.085	22.76	0.110	0.51	1.81	0.96	135	2.56
DC- 1400	1.50	0.010	132.69	0.380	0.39	1.91	1.17	135	2.56
Type C	1.90	0.011	111.10	0.555	0.354	1.72	0.71	170	2.95

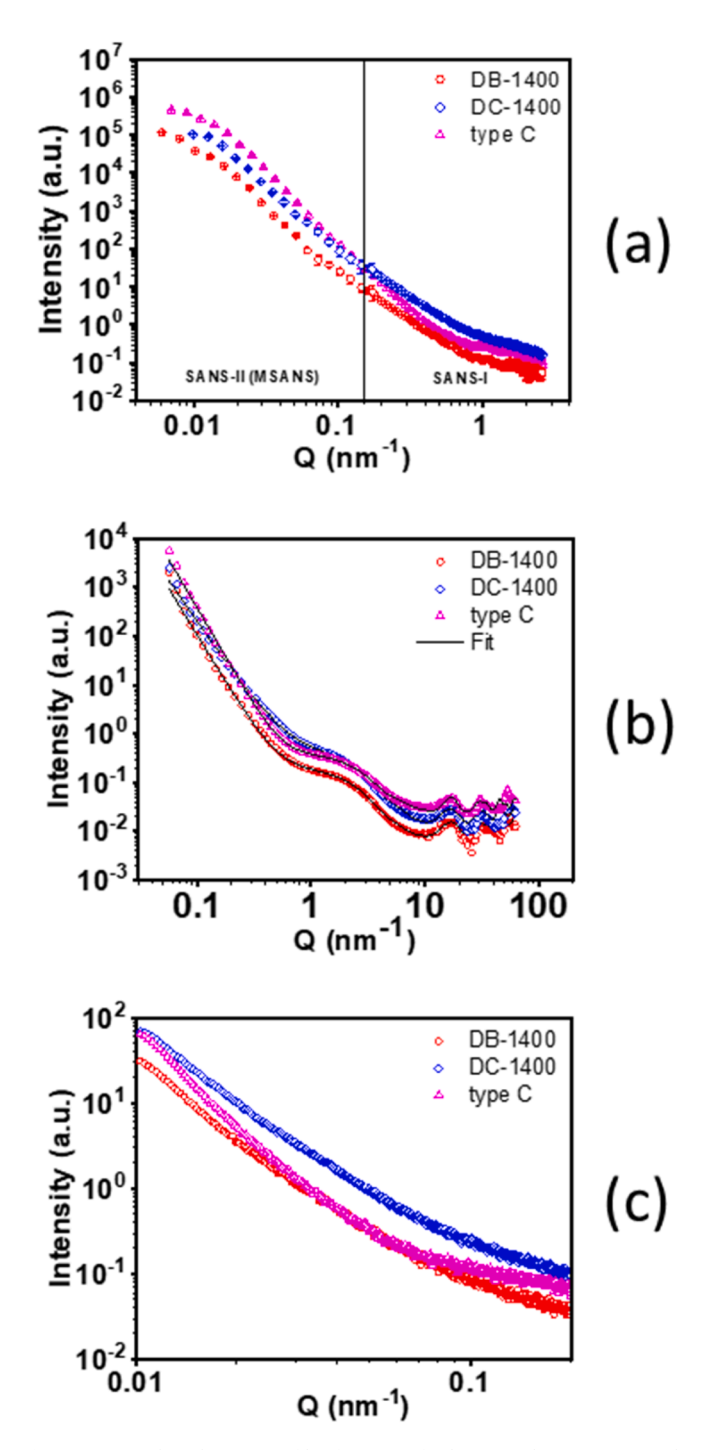


Fig. 6. (a) Combined SANS profiles from two facilities at Dhruva reactors; (b) the SANS profile TAIKAN, J-Parc; (c) SAXS data for DB-1400, DC-1400 and type C hard carbon samples.

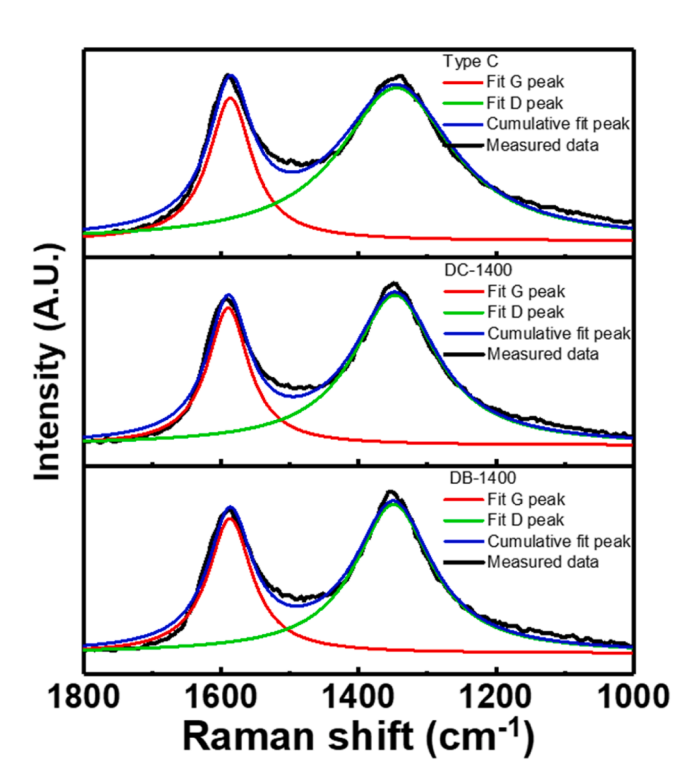


Fig. 7. Raman spectra of hard carbon samples DB-1400, DC-1400, and type C with fitting of D and G peak.

Table 2Fitted data from Raman spectra of HC samples.

Sample	Position of fitted D peak (cm ⁻¹)	Position of fitted G peak (cm ⁻¹)	I_D	I_G	I_{D}/I_{G}	L _a (nm)
DB- 1400	1349	1587	201.24	103.03	1.95	8.58
DC- 1400	1347	1590	222.40	98.98	2.25	7.46
C	1345	1586	303.03	107.86	2.81	5.96

(Fig. 8(c) and (d)) samples, DB-1400 and DC-1400 show the best cycling performance. That means, samples that are carbonized at the highest temperature (in the range of 1000 to 1400 $^{\circ}$ C) show better electrochemical performance. The extraction capacities and the Coulombic Efficiency (CE) for 1st and 2nd cycles can be found in Table 3.

Data in Table 3 shows that DB-1400 and DC-1400 have the best performance among all samples made from the same precursor. HC synthesized from bagasse samples generally possess better coulombic efficiency compared HC from dried corn waste. Especially, DB-1400 sample shows an initial coulombic efficiency of 89.0 %, which is considered very good compared to other reported HC samples derived from biomass [9-11,33]. DB-1400 shows a formation cycle capacity of 307 mAh/g with a reversible capacity of 301 mAh/g in the second cycle and for DC-1400 sample the value is 252 mAh/g and 250 mAh/g,

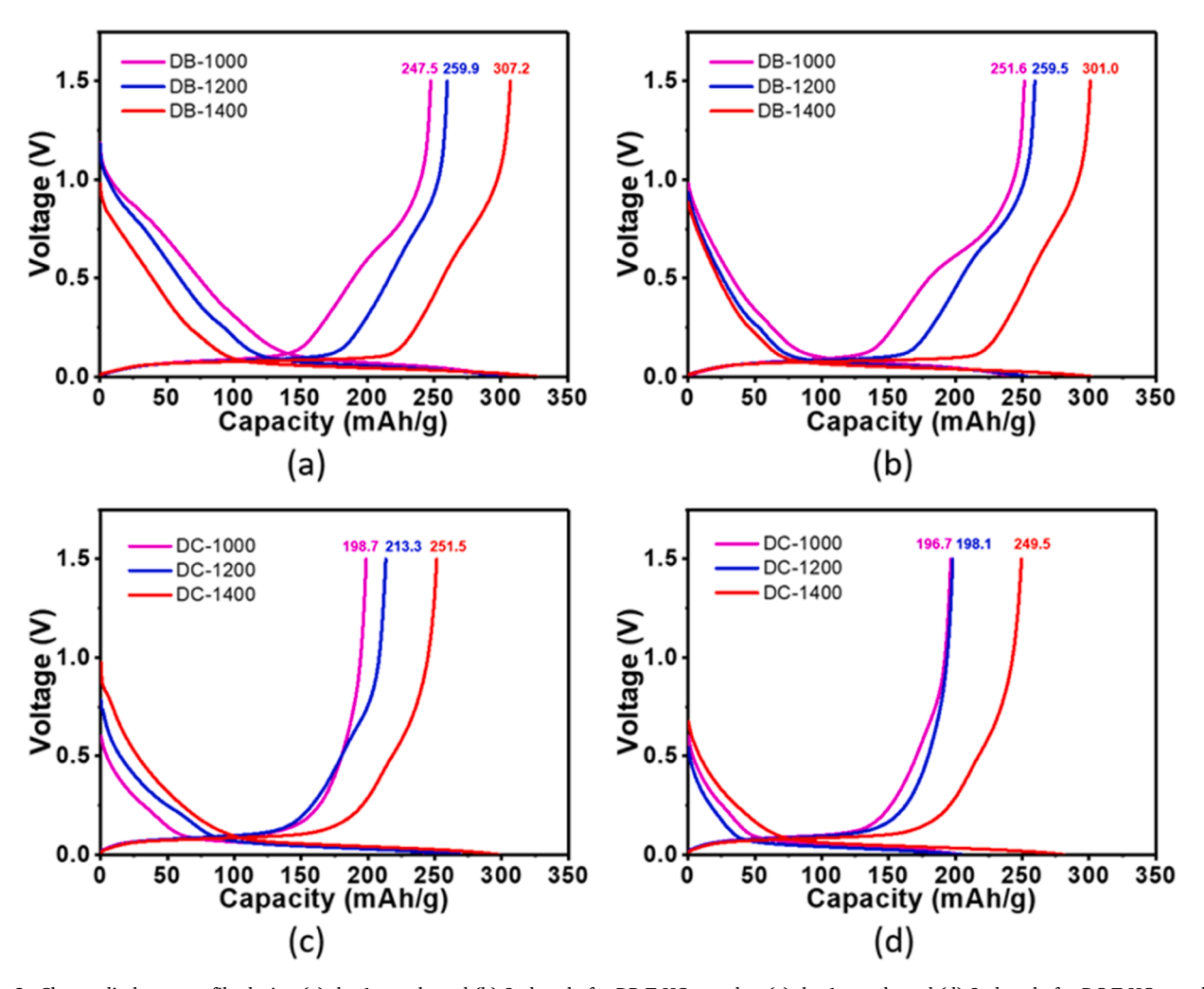


Fig. 8. Charge-discharge profile during (a) the 1st cycle and (b) 2nd cycle for DB-T HC samples, (c) the 1st cycle and (d) 2nd cycle for DC-T HC samples.

Table 3Capacity and coulombic efficiency of HC samples.

capacity and contonion emercincy of the samples.						
Sample	1st cycle capacity (mAh/g)	1st cycle CB (%)	2nd cycle capacity (mAh/g)	2nd cycle CB (%)		
DB- 1000	248	82.5	252	97.4		
DB- 1200	260	86.1	260	98.0		
DB- 1400	307	89.0	301	99.8		
DC- 1000	199	76.4	197	96.0		
DC- 1200	213	79.3	198	96.7		
DC- 1400	252	84.6	250	99.5		

respectively.

DB-1400 sample was chosen for high-rate performance study owing to its high storage capacity. The loading of the tested half-cell is 3 mg/cm², and the insertion rate for this half-cell is limited to C/2 rate since the focus is to investigate the extraction rate performance for the HC sample. Fig. 9(a) shows the voltage profile for the extraction process of DB-1400 sample at different C rate, and Fig. 9(b) shows the rate performance ν s. cycle number. The cell shows a reversible capacity of 307 mAh/g at C/10 and the capacity is retained at 234 mAh/g at 3C rate. The reversible capacity of the tested cell is very stable at each C rate.

Fig. 10 shows the long-term cycling performance of DB-1400 half cell

at a rate of C/2. Capacity retention of the tested half cell after 100 cycles is 93 % with an average coulombic efficiency of 99 %. DB-1400 sample has high sodium storage capacity as well as a really good capacity retention after long-term cycling comparing to similar studies [42-46]. Combining rate performance data and long-term cycling data can prove DB-1400 sample to be a promising candidate as anode material for high-rate SIB (full-cell).

From Fig. 11(a), the commercial HC sample (type C) shows a capacity of 275 mAh/g which is in between of DB-1400 (307 mAh/g) and DC-1400 (252 mAh/g). However, in term of the plateau capacity, type C sample shows the lowest value. Detailed value is shown in Fig. 11(b). The two regions in the extraction profile are attributed to two different sodium storage mechanisms in HC. In this work, results of tested HC samples suggest that they follow 'insertion-adsorption' sodium storage mechanism [47]. DB-1400, with the highest plateau capacity, demonstrates high sodium storage via insertion of Na⁺ in the pores formed in between small graphitic nano-domains. In order to achieve high plateau capacity, DB-1400 sample should have a loose structure constructed by small graphitic domains with large amount of mesopores in between [48]. On the other hand, the commercial sample shows highest slope capacity, which demonstrates high storage attributed to the intercalation of Na⁺ in the interlayer space between graphene sheets in the graphitic nano-domains. This result is in-line with the BET and BJH analysis showed earlier.

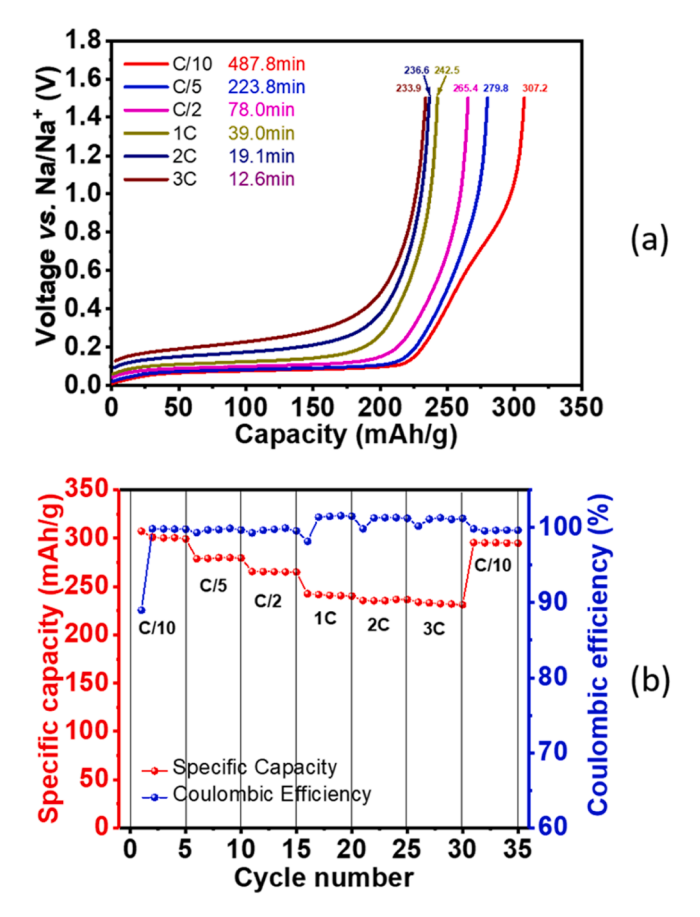


Fig. 9. (a) Rate performance of DB-1400 half-cell, and (b) rate performance and coulombic efficiency vs. cycle number.

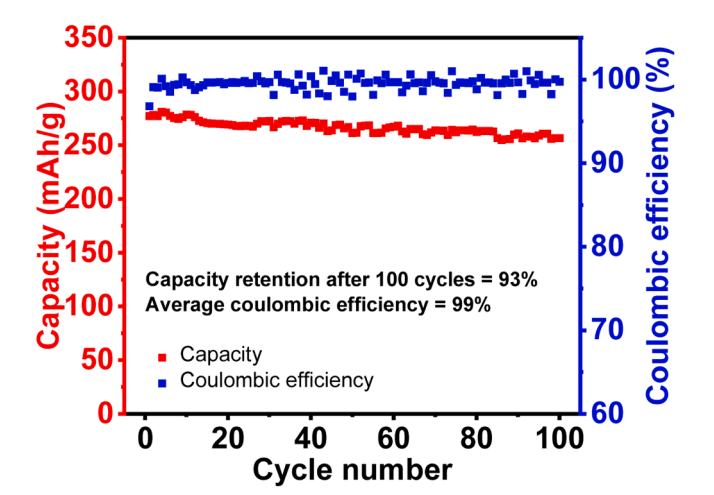


Fig. 10. Long-term cycling performance of DB-1400 half cell.

4. Conclusions

In conclusion, this work presents the sodium storage performance of two new lab-synthesized hard carbon materials prepared from different biomass precursors, and their material and electrochemical properties are compared to a commercially available hard carbon sample. The DB-1400 sample, derived from bagasse, delivers a storage capacity of 307 mAh/g at C/10 and retains its capacity at 234 mAh/g at 3C (with insertion rate of C/2). Compared to the other hard carbon samples synthesized from dried corn waste, DC-1400, and a commercial sample,

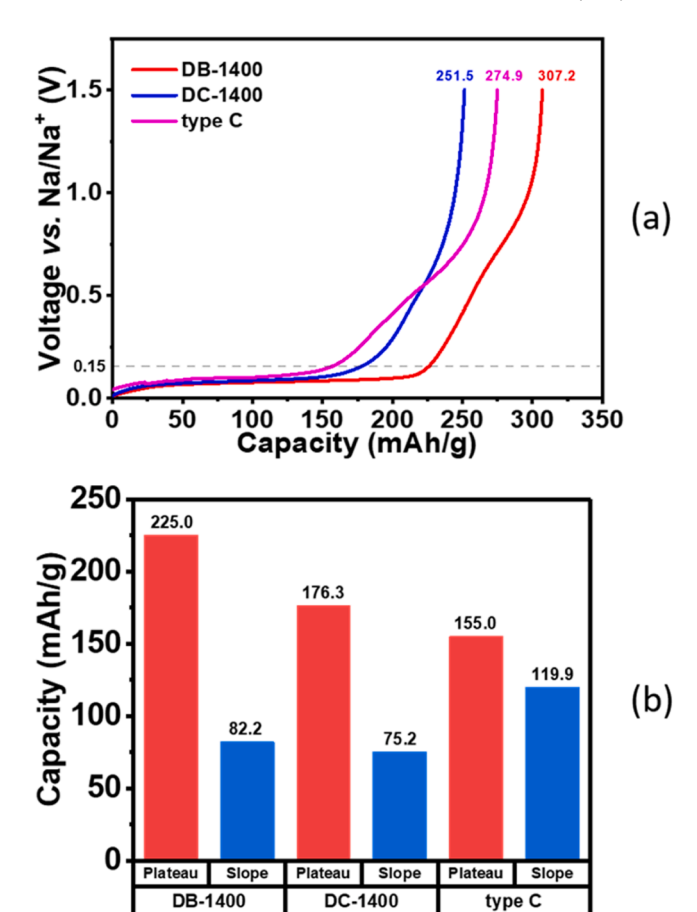


Fig. 11. (a) Extraction profile and (b) plateau vs. slope capacity comparison of different HC samples.

DB-1400 exhibits higher storage capacity with larger plateau capacity. This is in line with the results of structural characterization, *e.g.* BET, SAXS and SANS measurements. Based on the high rate-performance of DB-1400 sample, there is great potential of this HC material to be implemented as anode for high power sodium-ion battery.

CRediT authorship contribution statement

Chen Wang: Writing – original draft, Validation, Methodology, Investigation, Formal analysis, Data curation, Conceptualization. Debasis Sen: Writing – original draft, Validation, Methodology, Investigation, Formal analysis, Conceptualization. Vinod K. Aswal: Methodology, Investigation, Conceptualization. Lan Weiguang: Writing – review & editing. Palani Balaya: Writing – review & editing, Validation, Supervision, Resources, Project administration, Funding acquisition, Conceptualization.

Declaration of competing interest

The authors declare that they have no known competing financial interests or personal relationships that could have appeared to influence the work reported in this paper.

Acknowledgements

We sincerely thank Shin-ichi Takata for his help in SANS experiments at J-PARC, Japan. This research is supported by National Research Foundation, under the Energy Programme and administrated by Energy Market Authority (EP Award No. NRF2015EWT-EIRP002–017/WBS No R-265–000–568- 279).

Data availability

Data will be made available on request.

References

- [1] J.-Y. Hwang, S.-T. Myung, Y.-K. Sun, Sodium-ion batteries: present and future, Chem. Soc. Rev. 46 (12) (2017) 3529–3614.
- [2] D.A. Stevens, J.R. Dahn, The mechanisms of lithium and sodium insertion in carbon materials, J. Electrochem. Soc. 148 (8) (2001) A803.
- [3] B. Zhang, et al., Inhibitory activities of some traditional Chinese herbs against testosterone 5α -reductase and effects of Cacumen platycladi on hair re-growth in testosterone-treated mice, J. Ethnopharmacol. 177 (2016) 1–9.
- [4] H. Marsh, R. Menendez, et al., Chapter 2 Mechanisms of Formation of Isotropic and Anisotropic Carbons, in: H. Marsh, et al. (Eds.), Introduction to Carbon Science, Butterworth-Heinemann, 1989, pp. 37–73. Editors.
- [5] B. McEnaney, T.J. Mays, et al., Chapter 5 Porosity in Carbons and Graphites, in: H. Marsh, et al. (Eds.), Introduction to Carbon Science, Butterworth-Heinemann, 1989, pp. 153–196. Editors.
- [6] Z. Li, et al., Mechanism of Na-Ion Storage in Hard Carbon Anodes Revealed by Heteroatom Doping, Adv. Energy Mater. 7 (18) (2017) 1602894.
- [7] J.J. Kipling, et al., The pore structure and surface area of high-temperature polymer carbons, Carbon N Y 1 (3) (1964) 321–328.
- [8] E.R. Buiel, A.E. George, J.R. Dahn, Model of micropore closure in hard carbon prepared from sucrose, Carbon N Y 37 (9) (1999) 1399–1407.
- [9] J. Ding, et al., Carbon nanosheet frameworks derived from peat moss as high performance sodium ion battery anodes, ACS. Nano 7 (12) (2013) 11004–11015.
- [10] E.M. Lotfabad, et al., High-Density Sodium and Lithium Ion Battery Anodes from Banana Peels, ACS. Nano 8 (7) (2014) 7115–7129.
- [11] K.-L. Hong, et al., Biomass derived hard carbon used as a high performance anode material for sodium ion batteries, J. Mater. Chem. A 2 (32) (2014) 12733–12738.
- [12] J. Ding, et al., Peanut shell hybrid sodium ion capacitor with extreme energy-power rivals lithium ion capacitors, Energy Environ. Sci. 8 (3) (2015) 941–955.
- [13] N. Sun, H. Liu, B. Xu, Facile synthesis of high performance hard carbon anode materials for sodium ion batteries, J. Mater. Chem. A 3 (41) (2015) 20560–20566.
- [14] H. Li, et al., Carbonized-leaf Membrane with Anisotropic Surfaces for Sodium-ion Battery, ACS Appl. Mater. Interfaces 8 (3) (2016) 2204–2210.
- [15] M. Dahbi, et al., Synthesis of hard carbon from argan shells for Na-ion batteries, J. Mater. Chem. A 5 (20) (2017) 9917–9928.
- [16] C. Bommier, et al., Predicting capacity of hard carbon anodes in sodium-ion batteries using porosity measurements, Carbon N Y 76 (2014) 165–174.
- [17] Z. Guan, et al., Gelatin-pyrolyzed mesoporous carbon as a high-performance sodium-storage material, J. Mater. Chem. A 3 (15) (2015) 7849–7854.
- [18] W. Luo, et al., Low-surface-area hard carbon anode for na-ion batteries via graphene oxide as a dehydration agent, ACS Appl. Mater. &Interfaces (Providence) 7 (4) (2015) 2626–2631.
- [19] Z. Li, et al., High capacity of hard carbon anode in Na-ion batteries unlocked by POx Doping, ACS Energy Lett. 1 (2) (2016) 395–401.
- [20] H. Hou, et al., Large-area carbon nanosheets doped with phosphorus: a high-performance anode material for sodium-ion batteries, Adv. Sci. 4 (1) (2017) 1600243
- [21] J. Yang, et al., S-Doped N-Rich Carbon Nanosheets with Expanded Interlayer Distance as Anode Materials for Sodium-Ion Batteries, Adv. Mater. 29 (6) (2017) 1604108.
- [22] L. Xiao, et al., Low-Defect and Low-Porosity Hard Carbon with High Coulombic Efficiency and High Capacity for Practical Sodium Ion Battery Anode, Adv. Energy Mater. 8 (20) (2018) 1703238.
- [23] Y. Cheng, et al., The effect of thermal treatment temperature on the crystal structure and electrochemical performance of the coconut shell-based hard carbon, Solid State Jonics 402 (2023) 116374.
- [24] W. Song, et al., Mild Pretreatment Synthesis of Coal-Based Phosphorus-Doped Hard Carbon with Extended Plateau Capacity as Anodes for Sodium-Ion Batteries, SSRN Electr. J. (2023).

- [25] A. Kamiyama, et al., MgO-Template Synthesis of Extremely High Capacity Hard Carbon for Na-Ion Battery, Angewandte Chemie Int. Ed. 60 (10) (2021) 5114–5120
- [26] Rainey, T., A study into the permeability and compressibility of Australian bagasse pulp. 2009
- [27] Rose, J. The Rise of Industrial Corn Production. 2016; Available from: https://foodprint.org/blog/the-rise-of-industrial-corn-production/.
- [28] Corn Waste Potentially More Than Ethanol. 2006; Available from: https://www.sciencedaily.com/releases/2006/07/060719091421.htm.
- [29] V.K. Aswal, P.S. Goyal, Small-angle neutron scattering diffractometer at Dhruva reactor, Curr. Sci. (Bangalore) (2000) 947–953. Medium: X; Size: page(s).
- [30] S. Mazumder, et al., A medium resolution double crystal based small-angle neutron scattering instrument at Trombay, Curr. Sci. 81 (2001) 257–262.
- [31] S.-I. Takata, et al., The Design and q Resolution of the Small and Wide Angle Neutron Scattering Instrument (TAIKAN) in J-PARC, in: Proceedings of the 2nd International Symposium on Science at J-PARC? Unlocking the Mysteries of Life, Matter and the Universe?, 2015. Journal of the Physical Society of Japan.
- [32] A. Rudola, K. Du, P. Balaya, Monoclinic Sodium Iron Hexacyanoferrate Cathode and Non-Flammable Glyme-Based Electrolyte for Inexpensive Sodium-Ion Batteries, J. Electrochem. Soc. 164 (2017) A1098–A1109.
- [33] I. Izanzar, et al., Hard carbons issued from date palm as efficient anode materials for sodium-ion batteries, Carbon N Y 137 (2018) 165–173.
- [34] K. Sing, Reporting Physisorption Data for Gas/Solid Systems with Special Reference to the Determination of Surface Area and Porosity, Pure Appl. Chem. PURE APPL. CHEM. 54 (1982) 2201–2218.
- [35] I. Breßler, J. Kohlbrecher, A. Thünemann, SASfit: a tool for small-angle scattering data analysis using a library of analytical expressions, J. Appl .Crystallogr. 48 (2015) 1587–1598.
- [36] E. Walenta, Small angle x-ray scattering. Von O. GLATTER und O. KRATKY. London: academic Press Inc. Ltd. 1982. ISBN 0-12-286280-5. X, 515 Seiten, geb. £ 43,60; US \$ 81.00, Acta Polymerica 36 (5) (1985), 296-296.
- [37] J. Teixeira, Small Angle Scattering by Fractal Systems, J. Appl. Crystallogr. J. APPL. CRYST. 21 (1988) 781–785.
- [38] D. Saurel, et al., A SAXS outlook on disordered carbonaceous materials for electrochemical energy storage, Energy Storage Mater. 21 (2019) 162–173.
- [39] L.G. Cançado, et al., General equation for the determination of the crystallite size La of nanographite by Raman spectroscopy, Appl. Phys. Lett. 88 (16) (2006) 163106.
- [40] S. Komaba, et al., Electrochemical Na Insertion and Solid Electrolyte Interphase for Hard-Carbon Electrodes and Application to Na-Ion Batteries, Adv. Funct. Mater. 21 (20) (2011) 3859–3867.
- [41] V. Simone, et al., Hard carbon derived from cellulose as anode for sodium ion batteries: dependence of electrochemical properties on structure, J. Energy Chem. 25 (5) (2016) 761–768.
- [42] R. Muruganantham, F.-M. Wang, W.-R. Liu, A green route N, S-doped hard carbon derived from fruit-peel biomass waste as an anode material for rechargeable sodium-ion storage applications, Electrochim. Acta 424 (2022) 140573.
- [43] R. Muruganantham, et al., Bio-oil derived hierarchical porous hard carbon from rubber wood sawdust via a template fabrication process as highly stable anode for sodium-ion batteries, Mater. Today Energy 14 (2019) 100346.
- [44] R. Muruganantham, et al., Biomass Feedstock of Waste Mango-Peel-Derived Porous Hard Carbon for Sustainable High-Performance Lithium-Ion Energy Storage Devices, Energy Fuels 35 (13) (2021) 10878–10889.
- [45] D. Alvira, D. Antorán, J.J. Manyà, Plant-derived hard carbon as anode for sodiumion batteries: a comprehensive review to guide interdisciplinary research, Chem. Eng. J. 447 (2022) 137468.
- [46] J. Kuai, et al., Comparison and optimization of biomass-derived hard carbon as anode materials for sodium-ion batteries, Chem. Phys. Lett. 842 (2024) 141214.
- [47] X. Chen, et al., Understanding of the sodium storage mechanism in hard carbon anodes, Carbon Energy 4 (6) (2022) 1133–1150.
- [48] L. Yang, et al., Pore structure regulation of hard carbon: towards fast and high-capacity sodium-ion storage, J. Colloid Interface Sci. 566 (2020) 257–264.